Journal of Wind Engineering & Industrial Aerodynamics 271 (2026) 106387

Contents lists available at ScienceDirect

Journal of Wind Engineering & Industrial Aerodynamics

journal homepage: www.elsevier.com/locate/jweia

On-road pressure measurements on a full scale heavy-duty truck

I. Kurek [a], T. Castelain [a,*], M. Michard [a], D. Chacaton [b], S. Bholah [c], B. Pellarin [c]

[a] INSA Lyon, CNRS, Ecole Centrale de Lyon, Universite Claude Bernard Lyon 1, Laboratoire de Mécanique des Fluides et d'Acoustique, UMR5509, 69621, Villeurbanne, France
[b] Volvo Group Truck Technology, Renault Trucks SAS, Cab Engineering Lyon, 99 route de Lyon, 69806, Saint-Priest Cedex, France
[c] Lamberet SAS, 129 route de Vonnas, BP 43, 01380, Saint-Cyr-sur-Menthon, France

ARTICLE INFO

Keywords:
Aerodynamics
Experiments
Road vehicles
wake

ABSTRACT

An experimental study of the pressure distribution at the rear of a full tractor–trailer vehicle is presented. The influence of the underbody flow blockage is investigated. The measurements are performed using a differential pressure sensor. Stability of reference pressure during tests is required, and its knowledge allows to sort measurements in terms of reliability. A device is designed to measure the reference pressure and a corrective term allows it to be related to the atmospheric pressure in rolling conditions. The estimated repeatability of the measurements is around 1% for a reference underbody configuration. For various opening ratio of the underbody, changes in the overall pressure force on the rear surface, denoted by the product $S\langle\overline{C_p}\rangle$ between the area of the rear surface S and the spatial average of the pressure coefficient $\langle\overline{C_p}\rangle$, are mostly driven by the changes in rear surface. Finally, configurations with constant free spaces whose position are varying were considered. In this case, the vertical position of the free space is of primary importance for $S\langle\overline{C_p}\rangle$, with relative variations up to 18% between the lower and upper positions of the ground clearance free space.

1. Introduction

Aerodynamics of heavy-duty vehicles is a crucial point with respect to CO_2 emissions and fuel consumption or range. Among the differences compared to passenger cars aerodynamics, the underbody flow momentum is low, with a local velocity between 10% and 40% of the free flow velocity (Szmigiel, 2017), and the ratio between the height H and the width W of the vehicle, hereafter denoted as aspect ratio, is notably greater than one. The range of underbody flow velocity, which is quite large, is representative of the diversity of trailers configurations, with different uses of the free space in the underbody area (spare wheel storage for instance) and also different designs of the trailer rear, around the underrun protection device and the plate holder. For passenger cars as for trucks, laboratory-scale experiments emphasized wake flow characteristics, which are of primary importance as pressure drag is considered. The transposition to full-scale vehicles has already been performed in some cases. For instance, experiments on simple bluff bodies, aiming at reflecting general properties of passenger cars or light lorries, shed light on wake bistability (Grandemange et al., 2013a; Bonnavion and Cadot, 2018; Haffner et al., 2020; Ahmed and Morgans, 2023; Plumejeau et al., 2020), which corresponds to a wake reversal between two symmetrical states. This phenomenon is shown to have a significant effect on drag (Grandemange et al., 2013b) and has been observed on real vehicles during full scale tests in a wind tunnel (Grandemange et al., 2014; Bonnavion et al., 2019). Small scale experiments on variants of the well-known Ahmed Body with a varying ground clearance (Grandemange et al., 2013a; Fan et al., 2022) show that the induced variations of the underbody flow momentum lead to different wake topologies. The gradual change in wake topology led to the identification of four flow classes, for various Reynolds number values at small scale on a simplified heavy-duty vehicle geometry (Castelain et al., 2018). These classes can be distinguished one from the other by the pressure distribution at the model rear and the corresponding mean rear pressure value over the base. A brief description of the specific features of the different classes I to III is provided hereafter. In all cases, a vertical stratification of the base pressure is observed. For class I, obtained for low values of underbody flow momentum, the vertical gradient of pressure is slightly negative and small; it gradually increases with the underbody flow rate, up to a value at which the transition to class II occurs. For class II, the base pressure (in absolute value) is minimum, with a marked positive vertical pressure gradient. Transition to class III occurs as the underbody flow momentum is high enough to promote its interaction with the initial shear layer developing from the body top. This interaction is associated with a reduced vertical pressure gradient and a significant base pressure drop. Indeed, variations of around 20% of the mean rear pressure were found between flow classes II and III.

---

* Corresponding author.
E-mail address: thomas.castelain@ec-lyon.fr (T. Castelain).

https://doi.org/10.1016/j.jweia.2026.106387
Received 17 October 2025; Received in revised form 16 January 2026; Accepted 8 February 2026

Numerical simulations and full scale tests can answer the obvious need to transpose these results to the full scale. For numerical simulations, the challenge is to capture the effects of the complex geometry of the entire heavy-duty vehicle (mirrors, deflectors, A-pillars), as well as the obstruction of the underbody by various operational elements (axles, spare wheel, batteries, underrun protection device) on the underbody flow and wake development. In addition, it has been shown that the wake topology is highly sensitive to the numerical scheme used (Rao et al., 2018). Full scale wind tunnel tests are scarce in the case of heavy-duty vehicles; road tests are currently performed by manufacturers to assess the aerodynamic performance of vehicles (El-Alti et al., 2016), despite the technical difficulties associated with such measurements and the assumptions made to separate rolling resistance effects and drag.

The approach developed here thus concerns base pressure measurements on a full-scale truck on a test track, to focus on a major contributor to pressure drag. An objective is to answer the question of the transposition at full scale of the results obtained at lab-scale concerning flow classes and their properties (Castelain et al., 2018). Another aim concerns the evaluation of the measurement precision which dictates the ability of this experimental method to assess the aerodynamic performance of a given heavy-duty vehicle. In what follows, base pressure measurements are interpreted in terms of pressure coefficient C_p:

$$C_p = \frac{p - p_\infty}{\frac{1}{2}\rho U^2} \tag{1}$$

where p is the pressure, p_∞ is the static pressure of the undisturbed flow, equal to atmospheric pressure p_{atm} in the case of road tests, ρ is the density of air. U is the velocity of free flow from the point of view of the vehicle. The uncertainty on C_p is driven by the sum of three terms:

$$\frac{\Delta C_p}{C_p} = 2\frac{\Delta U}{U} + \frac{\Delta\rho}{\rho} + \frac{\Delta(p - p_\infty)}{p - p_\infty} \tag{2}$$

The first two terms in this sum, which are usually negligible in the case of wind tunnel tests, will be tackled here by specific complementary measurements. The third term of the sum, implying differential pressure measurements, is crucial because the pressure difference $p - p_\infty$ is expected to be small, of the order of 10 Pa. Its uncertainty is also influenced by the variable p_∞, which is easily obtained during wind tunnel tests but not accessible for road tests. Among the solutions to this problem, subtracting the spatial average of C_p eliminates any temporal variation in the reference pressure during a test and measures the temporal deviations of C_p (Cembalo et al., 2024). In the context of onboard measurements in a train (Gallagher et al., 2018), the reference pressure comes from a partially sealed tank located in the train, which only allows pressure fluctuations on a small time scale to be measured. Another approach (Wordley and Saunders, 2008; Wojciak, 2012) consists of measuring the static pressure at one point of a car hood, allowing a difference with p_∞ of less than 50 Pa to be obtained. This allowed cross wind gusts velocity measurements around the car, but was not used as a mean to perform parietal pressure measurements. Consequently, the above-mentioned approaches do not allow to measure an absolute value of C_p.

The objectives of this paper are therefore twofold: (i) to develop, set-up and apply a methodology of C_p measurements at the rear of a full-scale heavy-duty vehicle on a test track, including a sensitivity analysis of the error terms in Eq. (2); (ii) to explore different underbody closure configurations, simulating the protrusion into the underbody flow of operative elements of trailers, leading to various underbody flow velocities. This aims at determining the most favorable configuration from an aerodynamic viewpoint. The experimental set-up is presented in Section 2, and Section 3 focuses on the data processing to obtain the physical quantities of interest. The accuracy of the method will be explored in Section 4, and the results obtained for different underbody configurations will be presented in Section 5.

2. Experimental setup

2.1. Full scale truck and test track

The vehicle used for the measurements is a prototype of an extended electric tractor, similar to a T520 cab, coupled to a Lamberet SR2 trailer. This heavy-duty vehicle has a total length L = 16,955 mm, a height H = 2745 mm, and a width W = 2431 mm. Therefore the aspect ratio $H/W = 1.13$ is very close to that of small scale studies (Castelain et al., 2018). The terminal ground clearance at the rear back is G = 1103 mm, leading to $G/H = 0.40$. However, as the ground clearance is not constant along the trailer, and is significantly reduced below the tractor, this sole parameter may not be relevant for comparison with simplified models. The tests were carried out on the Renault Trucks proving ground located in La Valbonne (Ain, France). A 3250 m long test track, is dedicated to the evaluation of the performance of land vehicles. The results presented here are derived from a collection of measurements performed on a 900 m straight line on this track. A weather station is installed along this section, which measures the ambient temperature T_∞, and the atmospheric pressure p_∞. The mean wind velocity U_w and direction α are obtained from the Copernicus Climate Change Service for 1 h periods (Copernicus Climate Change Service, 2024).

As the wake signature on the rear back is investigated using pressure measurements, means of modifying it by altering the underbody flow are explored. The choice was made here to focus on modifications of the trailer rear end, by imposing a configurable blockage of the area directly below the trailer doors. The blocking device consists of up to 11 steel slats of height h_s of 100 mm each, the number and arrangement of which can be modified to allow for different configurations. Fig. 1 shows CAD of the obstruction system. The trailer is also equipped with lateral skirts or fairings to fully channel the underbody flow, as illustrated in Fig. 1.

2.2. Measurement chain

The general structure of the measurement chain is shown in Fig. 2; its description is developed here, before providing further detail in the following paragraphs on the specific subsystems that comprise it. The pressure taps are distributed across the rear of the trailer, according to a layout that will be detailed in Section 2.2.1. These ports are connected to a 32-channel multiplexed 1-kPa range differential sensor ESP-DTC-32 with 32 measurement pressure inputs (a given pressure input being denoted by p in what follows) and 1 reference pressure input (p_r), interfaced with a microDAQ (Chell) communication box, which is itself connected to an acquisition PC via an RJ45 interface. The sensor operates at an acquisition rate of 1000 Hz, allowing to limit measurement noise by averaging the data. To maximize the frequency response of the measurement chain, it is necessary to reduce the length of the tubing between the pressure ports and this sensor, which is therefore placed approximately half a meter away from the rear doors of the trailer. In addition, to compensate for sensor drift, on road equalization of the pressure between two input channels of the device has been set-up. This operation is called ‘rezero’ in what follows. The ESP-DTC-32 does not come with an in-house pneumatic built ‘rezero’ function, so an external set-up has been developed. It consists of a remote-controlled multi-channel pneumatic switch that allows the user to choose between two pneumatic states: measurement or reset. This system is designated as the “Zero pressure setting system” module in Fig. 2 and is composed of 33 electrically controlled solenoid valves. Fig. 3 shows the complete diagram of this chain. This diagram provides more details about the corresponding area depicted in Fig. 2, including wired communications (solid blue lines) and Bluetooth communications (dashed blue lines). Between two series of measurements, switching from ‘measurement’ mode to ‘rezero’ mode within 2 min is therefore possible.

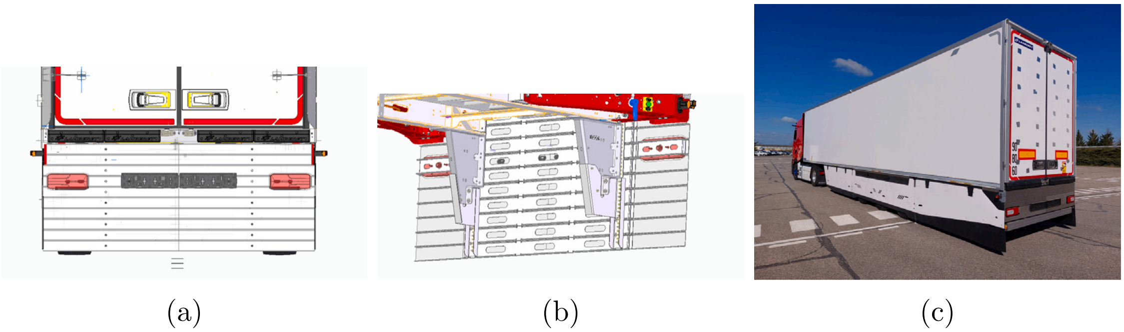

Fig. 1. CAD of the configurable obstruction system on the rear of the trailer. (a) rear view (b) view from inside the underbody showing the support system adapted with a vertical extension. (c) photograph of the vehicle.

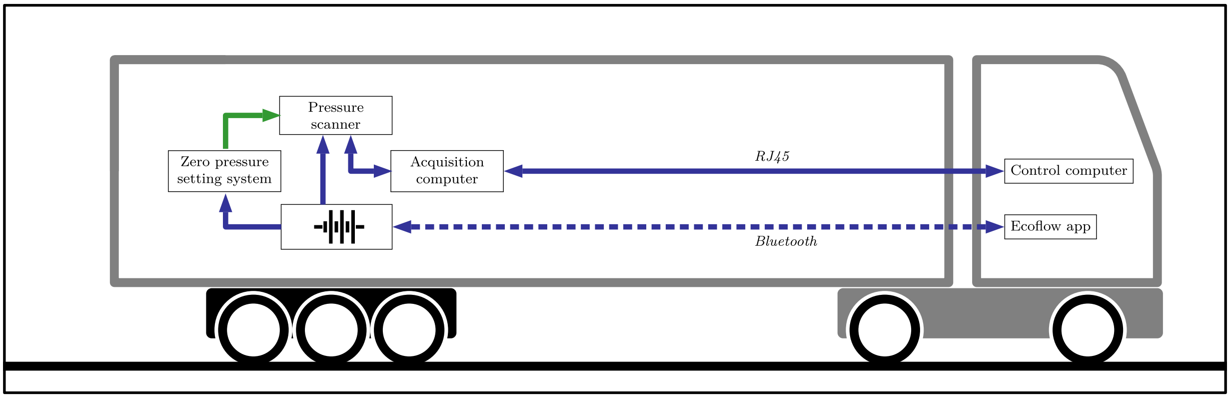

Fig. 2. General structure of the measurement chain on board the vehicle.

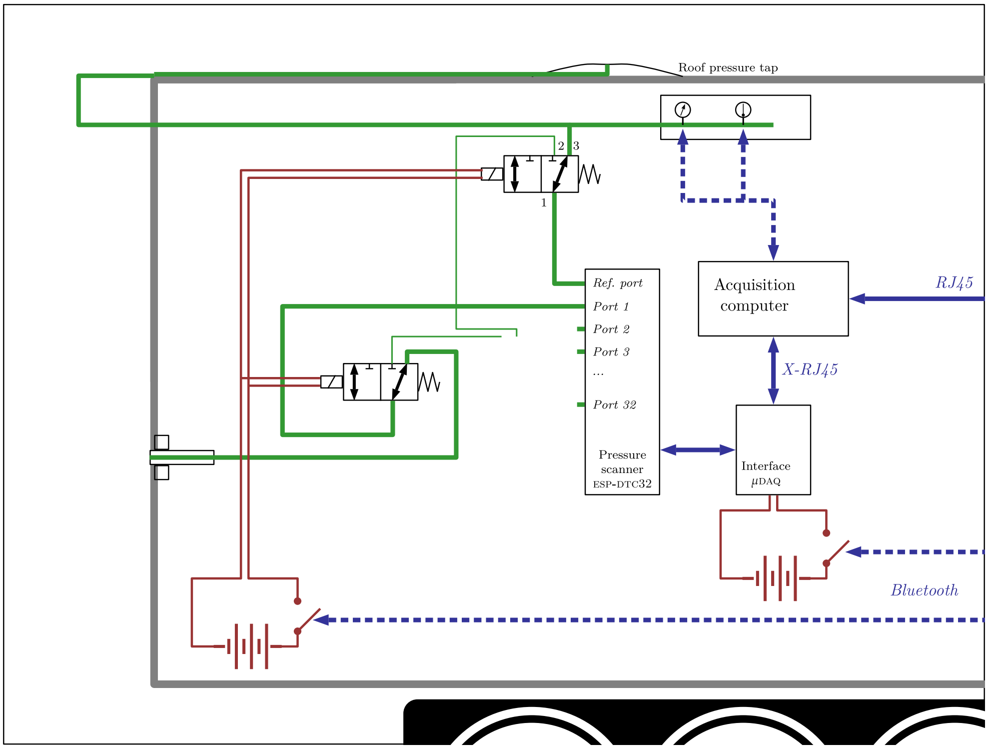

Fig. 3. Illustration of the entire pneumatic assembly.

2.2.1. Pressure measurements

Two types of pressure probes are used here. Tube-type probes are installed through the trailer doors. The doors are 88 mm thick so the tube outer diameter is quite large (15 mm). Its inner diameter, of 4 mm at the center is reduced to 1.5 mm at the measurement end, as shown in Fig. 4. The tubes are manufactured using SLS printing and are

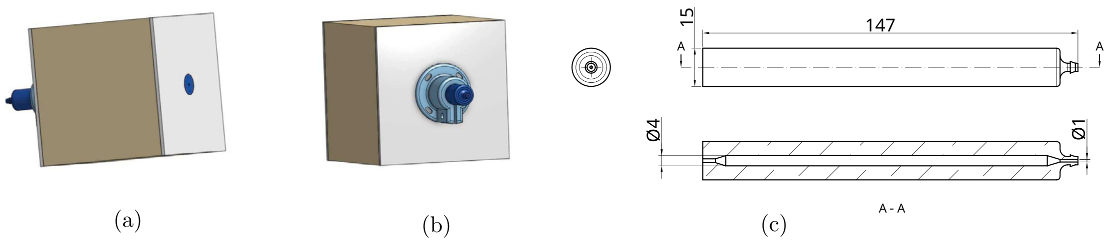

(a) (b) (c)

Fig. 4. Illustrations of the tube-type probe; (a) CAD view from outside the trailer (the cubic block corresponds to a sample of trailer rear door), (b) CAD view from inside the trailer, (c) sketch (dimensions in mm).

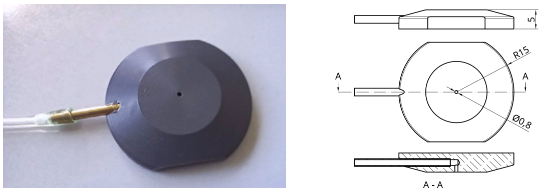

Fig. 5. Overview and layout of the pads-type probe (dimensions in mm).

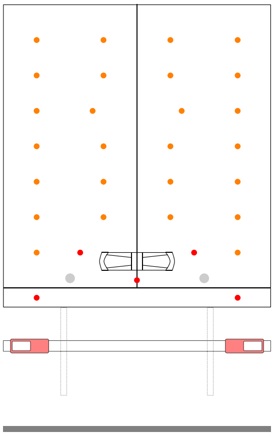

Fig. 6. Distribution of pressure taps. Fixed taps are shown in orange, while mobile taps are shown in red.

weatherproofed using a dedicated varnish. The end opening inside the trailer is connected to the pressure sensor via a flexible hose. In order to measure the pressure in the area of the trailer underbody obstructed by the slats, it was decided to develop a mobile device that could be placed on any slat as required, depending on the configuration studied. Five millimeter thick cylindrical pads with a non-through axial bore were designed and machined for this purpose. Fig. 5 illustrates this concept, similar to that used in Bonnavion et al. (2019). The flexible hose connected to the pneumatic outlet of this device is routed to the differential pressure measurement (inside the trailer) through one of the two holes provided for this purpose in the doors. The distribution of the pressure probes at the base is shown in Fig. 6, using a configuration without slats as an example. The baseline setup relies on 27 fixed pressure tube-type probes ans 5 pads.

As the time averaged pressure, noted $\overline{p}$, at different points over the trailer rear is considered in what follows, the question of the requested time of integration raises. It was previously shown that the spectral content of velocity fluctuations at the closure of the recirculation bubble gives rise to significant contributions around a frequency f made dimensionless by the height of the trailer, $St_H = fH/U$ of the order of 0.1 (Lahaye et al., 2014), and therefore a characteristic time τ for the wake of the order of $\tau \approx 10H/U$. To obtain a satisfactory temporal average, the pressure signal must be recorded over a sufficiently long time relatively to τ (typically 100 times greater). Measurements on a small scale model show a statistical convergence of the mean value, that is a difference of less than 0.1% with the mean value, from a minima of 300 τ. In our case, the minimum distance to be covered to satisfy this criterion is 8250 m, traveling at 25 m s^{-1}. Considering only the useful straight line of the test track (900 m), this corresponds to 9 passes.

The space average of pressure over the trailer rear is considered, as an indicator of the pressure drag due to wake development. Compared to atmospheric pressure, the average pressure $\langle\overline{p}\rangle$ exhibits a drop of around 100 Pa. In addition, the pressure difference between the top and bottom of the rear surface is also around a few tens of Pa. To be able to distinguish the values measured by the various probes distributed across the entire rear surface, it is therefore necessary to be able to distinguish values to within 10 Pa. Furthermore, one objective of this study is to highlight the changes induced on $\langle\overline{p}\rangle$ by changes in trailer configuration as described in Section 2.1. It can be expected that for moderate configuration changes (e.g., adding/removing a single slat), the changes in local pressure will be of the order of 1 Pa. The differential pressure sensor described in Section 2.2 was chosen for its capacity to measure such small pressure variations. For measurement accuracy in the order of 1 Pa, the reference pressure must be stable, to within this limit. The remaining question is thus reference pressure management, which is developed in the following section.

2.2.2. *Reference pressure*

This section describes the strategy used to handle the reference pressure, which should be stable and representative of p_∞. The stability of the reference pressure cannot be controlled, as it depends on atmospheric conditions but it is monitored throughout measurements. Indeed, to do so, a wall pressure probe is installed on the roof of the trailer to measure static pressure, and this probe provides the pressure information p_r, as illustrated in Fig. 3. The wall pressure could be measured using the same approach as for the rear of the trailer: drilling a hole and installing a tube identical to those shown in Fig. 4. This approach was rejected in order to preserve the integrity of the trailer body. A ‘tablet’ type probe is made with dimensions adapted to the flow encountered in this area of the trailer. Indeed, the probes used on the slats experience an average flow of low amplitude (of the order of 1 m s^{-1}), while the average flow developing on the roof of the truck is 25 m s^{-1} under the conditions envisaged for the tests. The roof tablet probe therefore has a much greater length-to-thickness ratio than ‘pads’ probes, so as to minimize its intrusiveness. The layout of this probe and a photograph of the model used are shown in Fig. 7, along with its sketch.

If p_r represents the reference pressure as measured by this device, this quantity can be linked to the pressure value of interest, which remains p_∞ as introduced in Eq. (1).

$$p_r = p_\infty + \Delta p_r \tag{3}$$

where Δp_r represents the difference between the static pressure in the roof area where the pressure probe was installed and p_∞.

RANS simulation of the flow around a reference heavy-duty vehicle provides the pressure distribution in the longitudinal symmetry plane of

(a) (b) (c)

Fig. 7. Roof tablet probe for wall pressure measurement; (a) CAD view, (b) photo of the printed probe, (c) sketch (dimensions in mm).

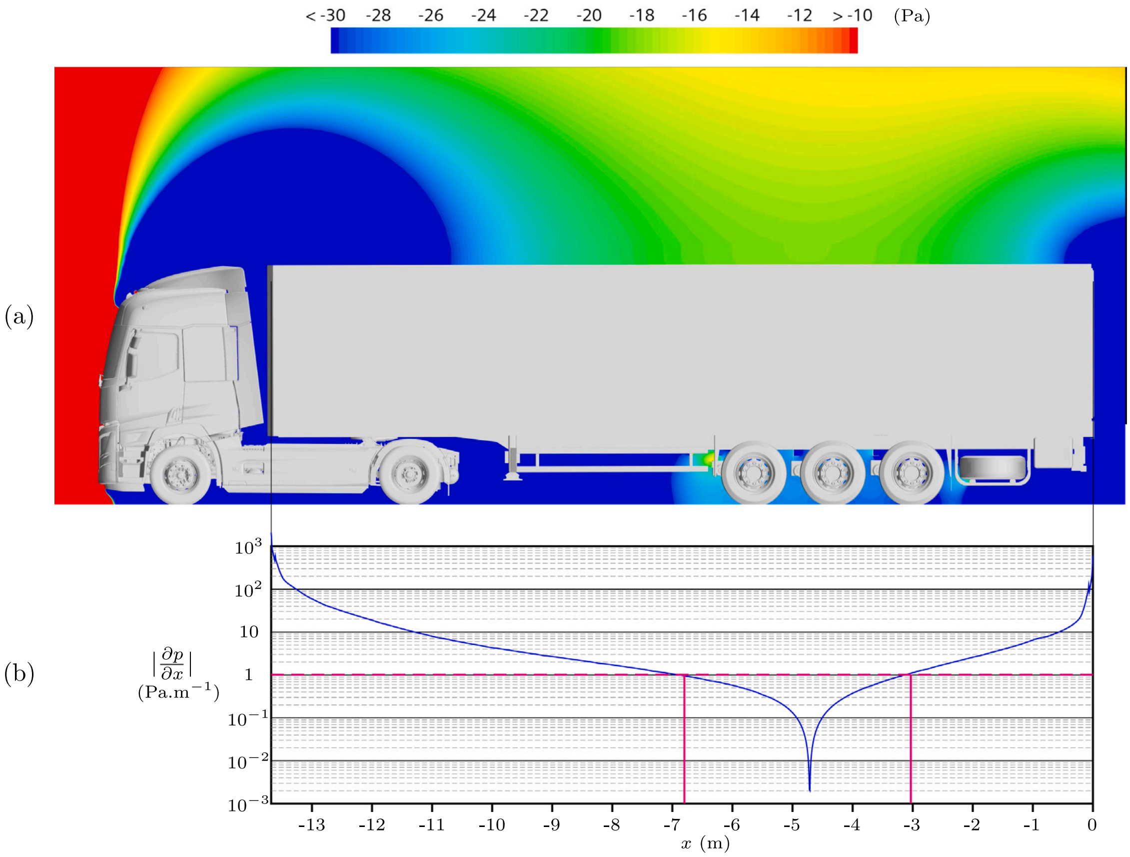

Fig. 8. (a) Pressure map around a typical heavy-duty vehicle, (b) pressure gradient on the roof of the trailer.

the vehicle shown in Fig. 8a. This simulation is performed according to the CFD methodology from Volvo AB and similar to the one described by Martini et al. (2011). The k-epsilon two layers turbulence model is used on a 100 million cells mesh. Prism layers are defined to better resolve the boundary layers (six layers on trailer's roof). This pressure distribution is used to determine the region of the trailer roof where the difference with the atmospheric pressure is minimal. This minimum is located approximately 4 m upstream of the end of the trailer, and it is at this distance that the pressure probe is installed. In addition, Fig. 8b shows that the pressure gradient along the axial direction x on the roof of the trailer is inferior to 1 Pa.m^{-1} in the area ranging from 7 m to 3 m from the rear of the trailer, as indicated by the blue lines. This ensures a certain flexibility on the placement of the probe. The pressure probe is connected to a sealed tank in which the pressure is measured by a Sparkfun Micro Pressure Sensor module, equipped with a Bosch Sensortech BMP581 sensor and interfaced with an Arduino Uno Rev4 Wifi board. The pressure information is transmitted via a Bluetooth connection to the acquisition computer (Fig. 3). One side of the tank is equipped with a nipple to connect a flexible hose, thus providing an outlet to the p_r input of the differential sensor. An empirical relationship between the velocity U and Δp_r is derived from dedicated measurements. These measurements were taken in windless conditions, therefore the vehicle velocity U_g with respect to the ground is considered to be equal to U in this case. Two examples of pressure signals recorded at U_g =25 m s^{-1} for this purpose are displayed in Fig. 9. Four time intervals are distinguished in this graph. The first plateau, in the interval noted (1), corresponds to the vehicle at rest at the beginning of the straight line, and therefore $p_r = p_\infty$. Interval (2) corresponds to an acceleration phase, until the stabilization of the vehicle velocity, which transcribes as a second pressure plateau in interval (3). The decrease of pressure during (4) is induced by a deceleration after the straight line. The pressure Δp_r in Eq. (3) is the difference between the averaged pressure of the two observed plateaus (1) and (3) in Fig. 9. This procedure was carried out for several velocities. The results of these measurements, displayed in Fig. 10, show a behavior in βU^2, with $\beta = -0.040$. Thus, leading to:

$$p_\infty = p_r + 0.040U^2 \tag{4}$$

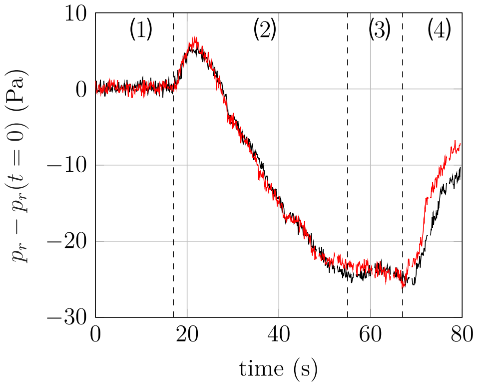

Fig. 9. Pressure signals recorded on the roof of the trailer with the vehicle at rest, an acceleration and a stabilized velocity $U_g = 25$ m s^{-1}.

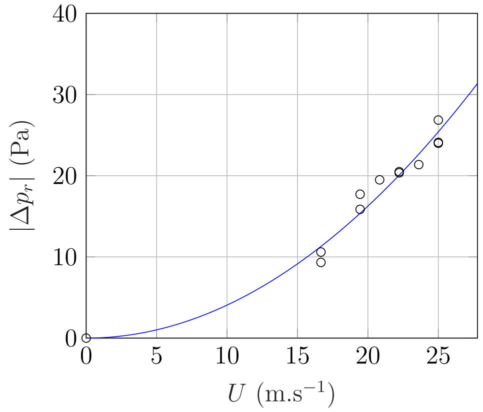

Fig. 10. Difference between the pressure measured at the roof and p_∞. ——: 0.040U^2, ∘: measurements.

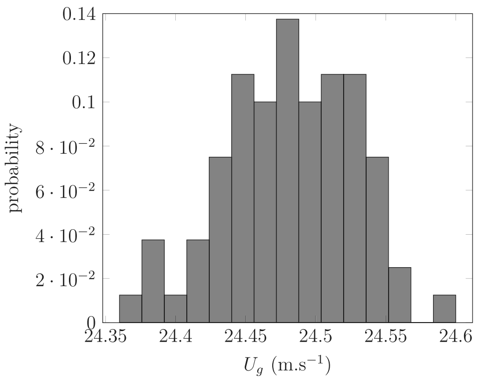

Fig. 11. Probability distribution of velocity U_g.

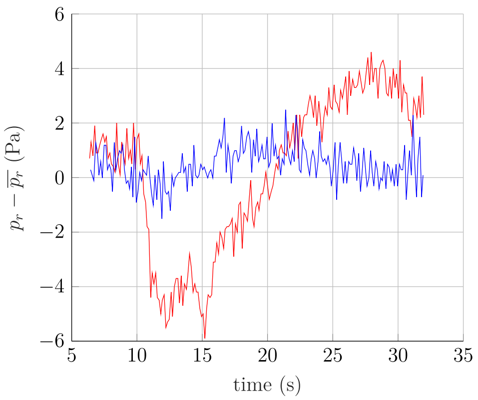

Fig. 12. Example of reference pressure signals p_r. ——: $\sigma(p_r) = 0.68$, ——: $\sigma(p_r) = 2.83$.

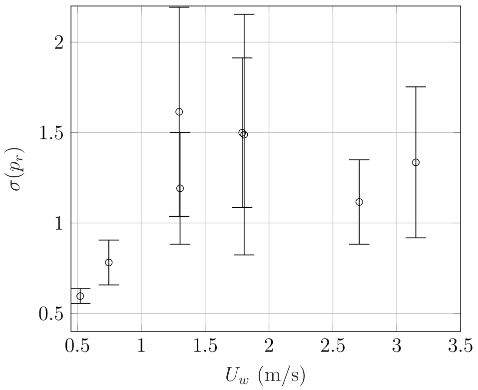

Fig. 13. Standard deviation of reference pressure $\sigma(p_r)$ for each run as a function of wind velocity U_w.

The coefficient β is derived from a least squares minimization of a quadratic function over 12 measurement points. Among these points, 11 are measured for various U_g, and 1 corresponds to the initialization of the sensor at $U_g = 0$ m s^{-1}. Two biases may be involved in the calculation of this coefficient. A first source of error would be due to limited number of measurements points used for the minimization. To address this issue, a statistical convergence test is performed on β by varying the number k of samples used within the set of the 11 measurement points for non zero values of U_g. The test is made using $k = 9$ and taking the 55 possible draws of the samples to be used. The mean value of β is 0.1% less than the value obtained with the complete data set. The standard deviation is 3.7×10^{-4} , or 1% of the mean value obtained with all samples. This uncertainty over β leads to an uncertainty of the atmospheric pressure of 0.25 Pa for $U_g = 25$ m s^{-1}, which is within the accuracy range of the pressure sensor. A second possible source of error is the individual accuracy of the measurement points. To estimate this error, an additional statistical study is carried out based on the complete set of measurement points. Simulated measurement noise is added to these data, on the basis of a random normal distribution of values between −1 and +1 Pa, and the coefficient β is recalculated from this degraded data set. From 100 generated data sets, the standard deviation of β is 3.5×10^{-4}, or 1% of the value obtained with the raw data. Therefore, the consequences of two possibles types of error on β are neglected in what follows.

The measurements performed to determine the empirical relationship between Δp_r and U have been made in no-wind conditions. However, care should be taken in windy conditions for two primary reasons. First, regardless of its direction, wind can induce a modification of p_r, or Δp_r, during the measurement. Second, for a given wind velocity, the relative orientation of the vehicle can induce a yaw, whose effect is not characterized. In Section 4, the precautions regarding these aspects are discussed.

3. Data treatment

This section details the data processing used to obtain, on the one hand, the mapping of $\overline{C_p}$ at the base and, on the other hand, the space averaged coefficient $\langle \overline{C_p} \rangle$. This process is carried out in two stages: data synchronization, and computation of the desired physical quantities from the raw data. The weather station data is recorded continuously

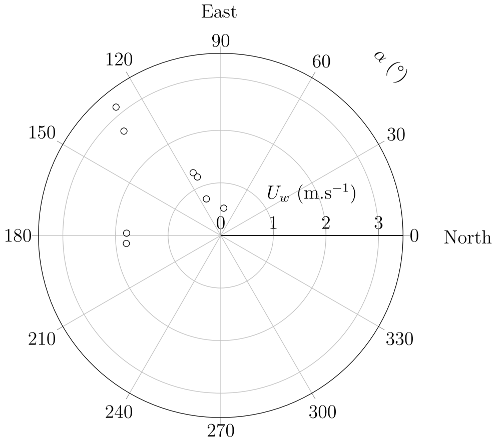

Fig. 14. Wind velocity magnitude U_w and direction α for the baseline case runs.

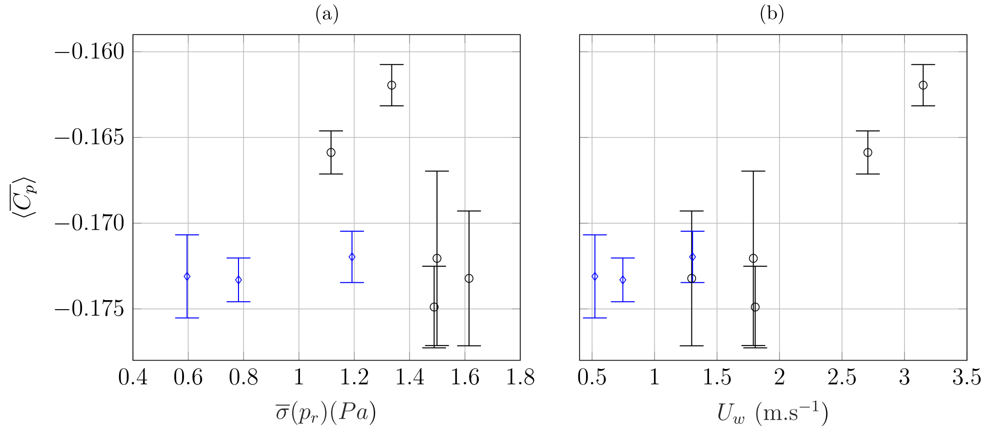

Fig. 15. Pressure coefficients obtained for each run as a function of their respective (a) mean $\sigma(p_r)$ and (b) mean wind velocity.

throughout the day. The rolling sequences are divided into *runs*, each consisting of 10 laps of the circuit. The “rezero” of the scanner is performed before the start of each run.

3.1. Data synchronization

The atmospheric pressure and temperature measurements p_∞ and T_∞, as well as the reference pressure p_r, are recorded with different computers on absolute time bases (computer clock) at different frequencies, around 0.01 Hz and 10 Hz respectively. It is therefore only necessary to interpolate them on the same time basis. The base pressure data are not synchronized on an absolute time basis, as the multi-channel sensor conditioner does not allow this. The time basis for the pressure sensor measurements is constructed using the sampling frequency, the recording duration, and the time at which the last recording was made (i.e., the file save time). This method only provides an approximation of the true time base of the pressure measurements, but this approximation is considered to be valid to within a few tenths of a second.

The aim is to look section per section at the data from the passages on the measurement straight section of the circuit. MATLAB’s datetime tag is used to record the times of passage at markers at the beginning and end of the straight section. From these tags, the speed U_g of the vehicle is estimated, and we deduce the times t_1 and t_2 between which the measured data are extracted for each lap.

3.2. Pressure coefficient computation

From the average temperature and atmospheric pressure measured during each section or pass, we can deduce the average density of the air during the acquisition on each section. Using the empirical law of Eq. (4), βU^2 is subtracted from the sensor’s pressure measurements to obtain $\Delta p_i = p_i - p_\infty$, which is used to calculate C_{p_i} (Eq. (1)) for each channel i of the sensor. The coefficient $\overline{C_{p_i}}$ is thus calculated for each scanner channel, averaged over the duration of the recording. The coefficient for each channel is interpolated over the base to obtain an interpolated map of the distribution of $\overline{C_p}$ at the base. This map is then spatially averaged to obtain the average pressure coefficient at the base $\langle\overline{C_p}\rangle$.

4. Baseline case

This section aims to present the results obtained on the configuration without added slats, in order to analyze the repeatability and the precision of the measurements. This configuration will be hereafter referred to as “baseline configuration”. In this configuration, 8 runs (80 passes) were made, on different weeks, times of day, and therefore different atmospheric conditions.

The velocity U_g of the vehicle with regard to the ground is measured for each passing on the straight line, as described in Section 3.1, even though the trailer speed regulator is used. It should be noted however that as the velocity is calculated from manually recorded time stamps, a random error is possible. Assuming a bias of a tenth of a second in the recorded time stamps leads to an error of approximately 0.5% on the velocity and thus 1% on C_p, as shown in Eq. (2). Fig. 11 shows the probability distribution of U_g for the measurements on the baseline configuration, from the 80 passes. The average value is 24.48 m s^{-1} and the standard deviation is 0.04 m s^{-1}, showing a satisfactory repeatability, that is 0.2% error. As the standard deviation of the Gaussian

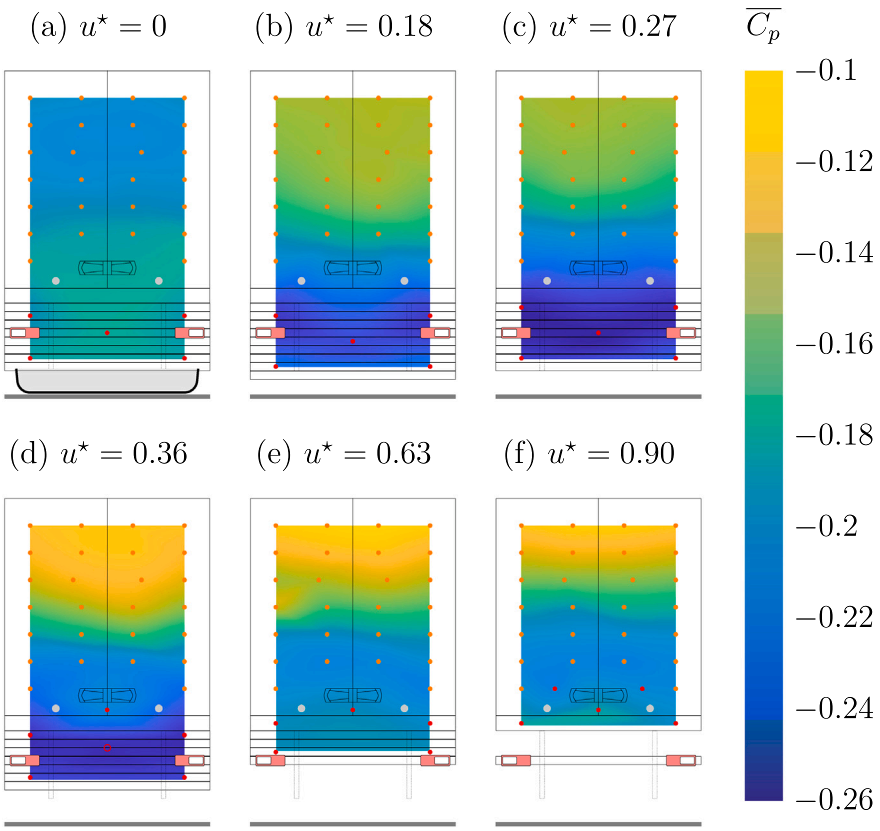

Fig. 16. Maps of $\overline{C_p}$ on the rear back for progressive obstruction of the underbody.

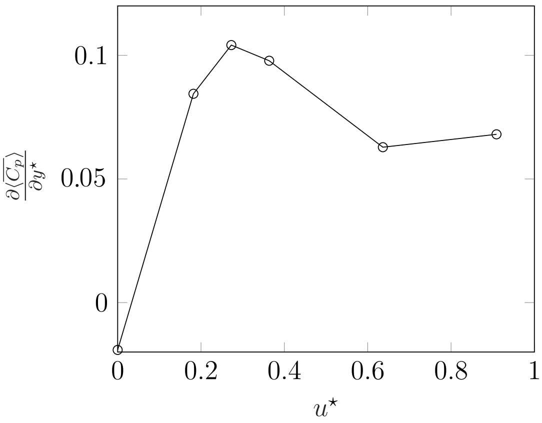

Fig. 17. Evolution of the vertical gradient of $\overline{C_p}$ with the underbody opening ratio.

distribution is of the order of what is expected owing to the procedure used to estimate U_g, the repeatability of real vehicle ground velocity from one section to the next one is in fact better than 0.2%. Therefore, in what follows, U_g is considered constant to 24.48 m s^{-1}, within 0.1% error.

Fig. 12 displays two reference pressure signals recorded in the sealed tank during two different measurements. Both signals show fluctuations, whose origin is attributed to changes in air speed with respect to the vehicle, due for instance to wind gusts. To quantify the level of fluctuations of this signal, its standard deviation σ is considered. For the samples presented in Fig. 12, a typical value of 0.68 for this indicator is associated with the case with no wind, and 2.83 is associated to windy conditions. The quantity $\sigma(p_r)$ will hereafter be an indicator to evaluate the stability of the reference pressure.

Fig. 13 shows the values of $\sigma(p_r)$ for each run as a function of U_w extracted from the Copernicus data set (see Section 2). The error bars correspond here to the standard deviation of $\sigma(p_r)$ at each value of U_w. The noticeable feature is that for low wind velocity, typically below 1 m s^{-1}, both $\sigma(p_r)$ and its dispersion are lower than for high values of U_w. These results indicate that a low $\sigma(p_r)$, typically below 1 Pa, is indicative of stable reference pressure. Fig. 14 displays the mean wind velocity U_w and its direction α with respect to the north, measured during each run. The dominant wind is between 90° and 130°, that is in direction of the south-east. As the measurements are performed on a east-to-west straight line, it means that the vehicle is facing a headwind is most cases. Therefore, the velocity with respect to the ground U_g underestimates the velocity U of air with respect to the vehicle. In the following, an estimate of velocity U, based on a projection of U_w on the vehicle axis, is introduced :

$$U = U_g + \sin(\alpha)U_w \tag{5}$$

The pressure coefficients obtained for each run are shown in Fig. 15 as a function of their respective mean $\sigma(p_r)$ (Fig. 15(a)) and wind velocity (Fig. 15(b)). Fig. 15(a) shows a weak dependency of the mean value of $\langle\overline{C_p}\rangle$ for each run, except two outliers, whose values are above −1.70. However, $\sigma(\langle\overline{C_p}\rangle)$, represented by the error bars, tends to increase with $\sigma(p_r)$, indicating that the measurements in each run show more disparity. Fig. 15(b) shows a plateau of $\langle\overline{C_p}\rangle$ around −0.173, up to U_w = 2 m s^{-1}. Then, $\langle\overline{C_p}\rangle$ tends to increase with U_w, reaching −0.162 for U_w = 3.1 m s^{-1}. This indicates that for low values of wind velocity, the measurement of $\langle\overline{C_p}\rangle$ is robust. For $U_w > 2$ m s^{-1}, as the wind is not in the axis of the vehicle, the yaw angle of the fluid might modify the wake and therefore induce higher values of $\langle\overline{C_p}\rangle$. Although

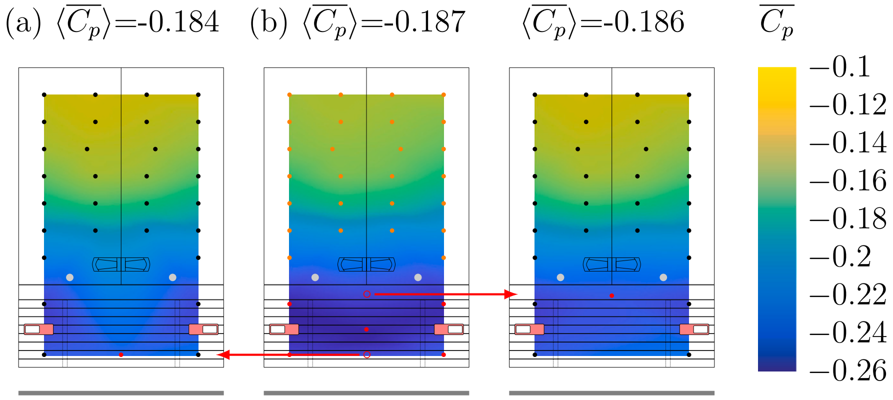

Fig. 18. Maps of $\overline{C_p}$ on the rear back for different central pad positions.

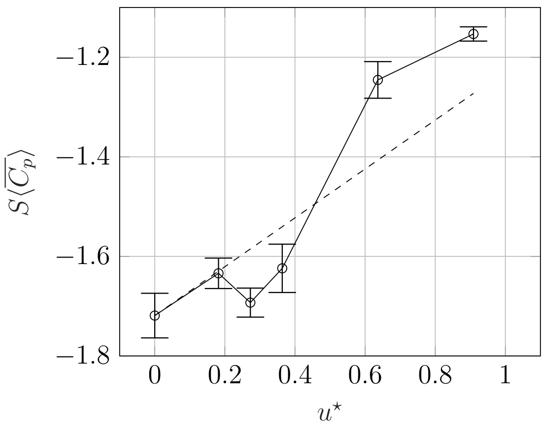

Fig. 19. Evolution of $S\langle\overline{C_p}\rangle$ and $S^\star$ with the underbody opening ratio.

the values of U are corrected to take into account the wind velocity, only values averaged over one hour were available. Therefore in case of strong winds above 2.5 m s^{-1}, a long average is less representative of wind conditions, that are prone to vary over shorter time-scales, for instance between the recording over one section and the following one. This explains two runs that stand out in Figs. 15(a) and 15(b), that correspond to high values of U_w. In order to obtain the most reliable value of $\langle\overline{C_p}\rangle$ for a given configuration, runs with too high values of $\sigma(p_r)$ or U_w must be discarded. Given the atmospheric conditions of the experiments, the limit is set to $\sigma(p_r)$ superior to the mean value of $\sigma(p_r)$ on all the runs for a given configuration (1.2 in this case), and $U_w > 2$ m s^{-1}. For the baseline case, three runs are retained (in blue with diamond symbols in Fig. 15), that is 30 passes, giving the final value of $\langle\overline{C_p}\rangle = -0.1728 \pm 0.0019$.

5. Underbody obstruction

In this section, various underbody configurations are explored. They differ one from the other by their opening ratio, $u^\star$, defined as the ratio between the free space at the trailer rear and the terminal ground clearance :

$$u^\star = \frac{(11-n)h_s}{G} \tag{6}$$

with n varying from 1 to 11 being the number of added slats, the individual height of which is noted h_s. The total rear surface S to be taken into account for evaluating the resulting pressure force is thus :

$$S = [H + G(1-u^\star)]W \tag{7}$$

The term $S\langle\overline{C_p}\rangle$ will thus be considered in this section as an indicator of the drag force at play in each configuration. First, the effect of $u^\star$ on $S\langle\overline{C_p}\rangle$ will be studied, with a location of free space at the lower part of the trailer rear. Second, configurations with constant $u^\star$ but different locations of the free space will be considered.

5.1. Progressive underbody opening ratio

Fig. 16 shows the pressure distribution on the rear back of the vehicle, with varying $u^\star$. The first case (Fig. 16a) is fully closed and is similar to the distribution reported by Castelain et al. (2018) for class I flows. Indeed, the distribution is rather homogeneous, with a slight maximum of pressure on the lower part. The other cases are consistent with class II flows, with a pressure maximum on the top half of the rear back, that is more prominent with the opening ratio. Note that to obtain the pressure distribution in Fig. 16d, a synthetic pressure tap was added (red circle). The pressure attributed to this synthetic point is equal to the pressure on the edge of the rear at the same height, from the interpolated cartography without this new point. It was done to ensure the vertical stratification that is observed on every other configuration, but was not reproduced by the interpolation in this case, due to an insufficient discretization in the slat area. As the distributions are vertically stratified, the vertical pressure gradient $\frac{\partial\langle\overline{C_p}\rangle}{\partial y^\star}$ can be viewed as an indicator of wake structure. It is defined by:

$$\frac{\partial\langle\overline{C_p}\rangle}{\partial y^\star} = \frac{\langle\overline{C_p}\rangle_{h1} - \langle\overline{C_p}\rangle_{h2}}{(y_1 - y_2)/(H_{tot})} \tag{8}$$

with $\langle\overline{C_p}\rangle_{hi}$ the horizontal mean of $\overline{C_p}$ at altitude y_i. In each case, y_1 and y_2 are arbitrarily located 80 mm below the top and above the bottom of the interpolated pressure distribution. H_{tot} is the total height of the rear back, that is H plus the height of the added slats. The obtained vertical gradients are shown in Fig. 17. The fact that the $u^\star = 0$ (fully closed) configuration leads to a wake of class I is confirmed by the negative value of the gradient. The other configurations show increasing values of the vertical gradient up to 0.1 for $u^\star = 0.36$, and then a slight decrease, down to 0.07 for $u^\star = 0.90$. These values are consistent with that derived from small scale measurements with class II flows. Even though a systematic comparison between the results at low scale (Castelain et al., 2018) and the present results at full scale should be performed cautiously, notably because the modification of the underbody flow results from different strategies between the two studies, a parallel can be drawn between the decrease in vertical gradient with the opening ratio at full scale and a similar behavior at low-scale (Castelain et al., 2018) for values of the parameter λ leading to a transition towards flows of class III.

One may note that as the number of sensors is fixed, an increase of the number slats used corresponds to a decrease of the spatial resolution

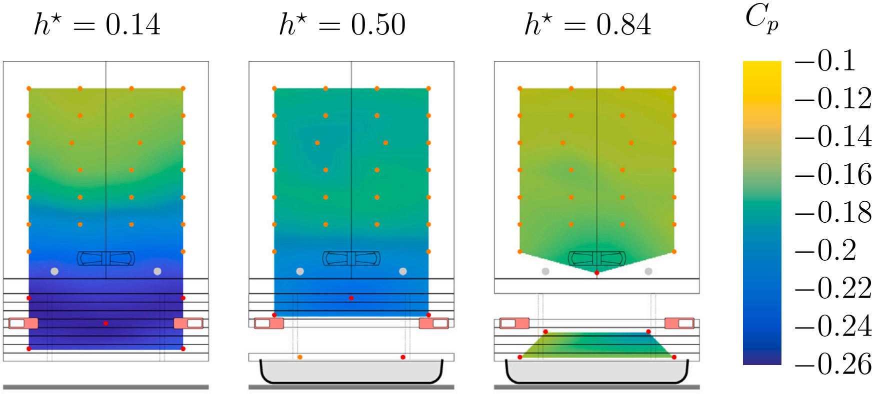

Fig. 20. $\langle\overline{C_p}\rangle$ distributions for three slats free space configurations.

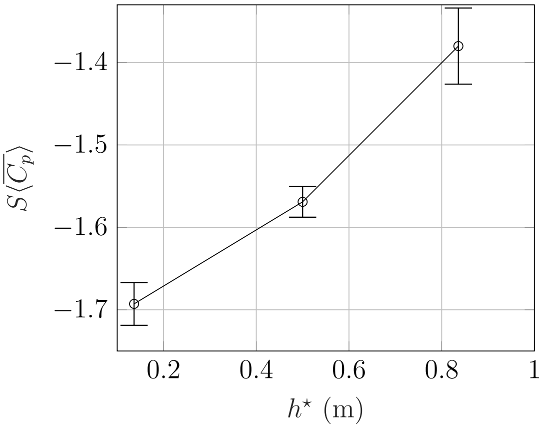

Fig. 21. Evolution of $S\langle\overline{C_p}\rangle$ with $h^\star$ for three slats free space configurations.

of the pressure measurement over the slats. This is particularly clear for configurations with several slats below the traffic light (Fig. 16(a-d)). The pressure data interpolation in this case relies on few measurement points, and the question raises of how the interpolation process in this area may influence the spatial average for pressure coefficient $\langle\overline{C_p}\rangle$. A heuristic approach has been considered here to tackle this point, on the basis of pressure measurements obtained for any trailer configuration. As an example, the configuration of Fig. 16c is considered. The pressure data is interpolated over the trailer rear which provides a pressure field that is considered in what follows to be the true (exact) pressure field. On this basis, a new set of 'pseudo' measurement points is chosen and the corresponding pressure values are extracted from this field. They are used to evaluate the resulting spatially averaged pressure coefficient $\langle\overline{C_p}\rangle$ after a new interpolation between the 'pseudo' data. In Fig. 18b, this process relies on the actual measurement points. In Fig. 18a, the central pad (in red in Fig. 18b) is replaced by a pseudo data point located at the bottom limit of the pressure field; on the contrary, in Fig. 18c, it is replaced by a pseudo data point near the upper slat. Thus all the measurements points, except one (that of the central pad) are used in Figs. 18a and 18c. These two extreme cases correspond to the worst case scenarios for $\langle\overline{C_p}\rangle$ evaluation. The difference in results obtained with this process is used as an indicator of the error due to the discretization/interpolation process, which acts independently from the error due to measurement noise. For the configuration of Fig. 18b, the estimated maximum error ΔC_p due to interpolation/discretization is set to 0.003, namely the largest difference between the results presented in Fig. 18. The process is applied to each trailer configuration and the results in Figs. 19, 21 and 23 come along with error bars whose magnitude is defined as $\pm S\sqrt{\sigma(\langle\overline{C_p}\rangle)^2 + \Delta C_p^2}$, with $\sigma(\langle\overline{C_p}\rangle)$ the standard deviation of $\langle\overline{C_p}\rangle$ evaluated over 20 passes (30 passes for the $u^\star$=0.91 case in Fig. 19).

Fig. 19 shows the evolution of $S\langle\overline{C_p}\rangle$ with $u^\star$. The value of $S\langle\overline{C_p}\rangle$ increases with $u^\star$ almost linearly. It varies from −1.71 for the 0.18 opening ratio case to −1.15 for the most open case, which corresponds to a relative gain of 32%. The variation of S between these two different cases ranges from 8.86 m^2 to 6.67 m^2, corresponding to a surface decrease of 24%. Therefore, the change in surface is of higher importance compared to $\langle\overline{C_p}\rangle$ variations, regarding the drag force. The evolution of $S^\star = -(S/S(u^\star = 0))S\langle\overline{C_p}\rangle(u^\star = 0)$ is also shown in Fig. 19 in dashed line. This shows the evolution that $S\langle\overline{C_p}\rangle$ would have in the case of an identical distribution to that of Fig. 16a, scaled on a varying surface S. Values of $S\langle\overline{C_p}\rangle$ for $u^\star < 0.4$ are below this tendency, but are higher for increasing $u^\star$. This indicates that independently of the considered surface, configurations for which $u^\star > 0.5$ are more efficient in terms of $\langle\overline{C_p}\rangle$. This observation raises the question of the evolution of $S\langle\overline{C_p}\rangle$ for a unique value of $u^\star$, thus a unique value of S, but different free space positions. This will be investigated hereafter.

5.2. Constant opening area

Configurations with a constant opening area are explored here. Two and three slat (200 mm and 300 mm) free spaces whose position are varying are considered. When the surface S is not continuous, which is the case for most of the configurations investigated in this section, the pressure coefficient applying on each surface $\langle\overline{C_p}\rangle_i$ is considered, such as:

$$S\langle\overline{C_p}\rangle = S_t\langle\overline{C_p}\rangle_t + S_b\langle\overline{C_p}\rangle_b \qquad (9)$$

with the subscripts t and b referring to the top and bottom of the rear back respectively. Also, in configurations where the pressure distribution over S_b is investigated by use of two pads only, the mean value given by the sensors is used to evaluate $\langle\overline{C_p}\rangle_b$. Fig. 20 shows pressure distributions for the three slat free space. For the left case where the free space is close to the ground, the pressure distribution exhibits a maximum at the top of the rear base. However, as the free space is moving up, the distribution tends to be more homogeneous, and the pressure maximum is pushed downwards. For smaller scale experiments, measurements by Cadot et al. (2015), Castelain et al. (2018) show velocity profiles with a maxima at mid-height at the exit of the underbody. On a real trailer configuration, it might not be the case, due to the presence of an axle and different elements in the underbody. Therefore, the blockage effect by the slats might be twofold. First, a potential effect on the underbody flow, creating less momentum, and second, a blockage of an area where the flow velocity is maximum in the baseline case. In both cases, the effect is a disruption of the

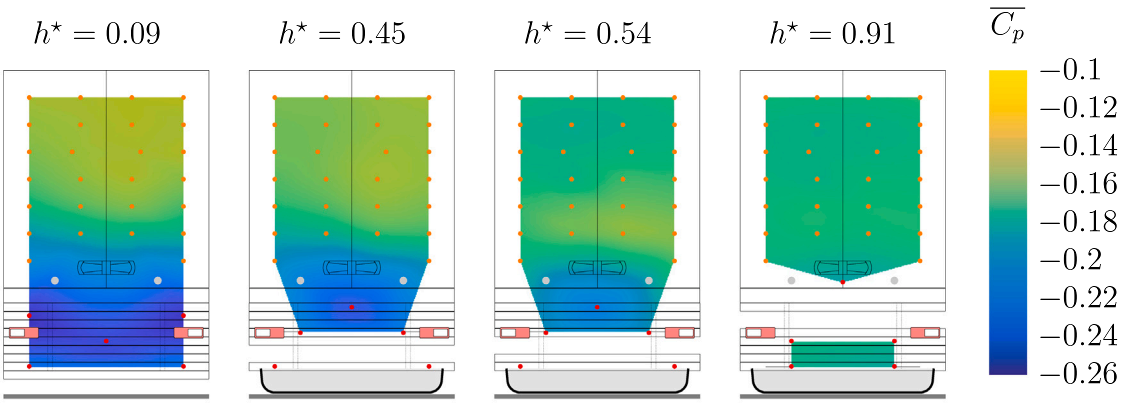

Fig. 22. $\langle\overline{C_p}\rangle$ distributions for two slats free space configurations.

backflow on the rear base, leading to flows similar to class I. Fig. 21 shows the evolution of $S\langle\overline{C_p}\rangle$ with $h^\star = h/G$, h being the mid-height of the free space. As the surface S is constant, the variations are only caused by changes in $\langle\overline{C_p}\rangle$. We observe an increase in $S\langle\overline{C_p}\rangle$ with the height of the free space, with $S\langle\overline{C_p}\rangle \simeq -1.69$ for the low position and $S\langle\overline{C_p}\rangle \simeq -1.38$ for the high position, corresponding to an increase of 18%.

Moving on to the two slats opening cases, a similar effect on the pressure distributions is shown in Fig. 22. As the number of possible configurations is geometrically higher in this case than in the previous one, the downward progression of the pressure maxima is more easily observable. Fig. 23 displays the evolution of $S\langle\overline{C_p}\rangle$ with $h^\star$ for these cases. As with the three slats opening, $S\langle\overline{C_p}\rangle$ increases with $h^\star$. It is equal to -1.63 for $h^\star = 0.9$, and increases up to -1.47 for $h^\star = 0.1$, that is a gain of 10%.

In the different configurations tested here, the overall pressure force on the rear surface, depicted by the variable $S\langle\overline{C_p}\rangle$, proved to be significantly higher as the opening is located in the ground proximity. In road transport by lorry, some of the components located at the rear of the trailer (e.g. underrun protection device, number plate holder, rear lights) are positioned in accordance with regulatory requirements. Their presence creates an obstruction to the flow, the position and size of which can be changed only marginally. However, in addition to these regulatory elements, there are also optional elements (splash guards, additional plates) that are the result of design choices or trailer customization, as depicted in Fig. 24 where a short sample of the galaxy of different configurations is provided. The experimental results presented in this section indicate that a minimization of the overall blockage (Section 5.1) and a location of the residual blockage in the higher part of the underbody (Section 5.2) are coupled with a decrease of the overall pressure force on the trailer rear. Complementary measurements of the global drag force (that would then include the pressure force component on the inner part of the different slats) would be particularly useful to establish the drag net gain associated with these recommendations.

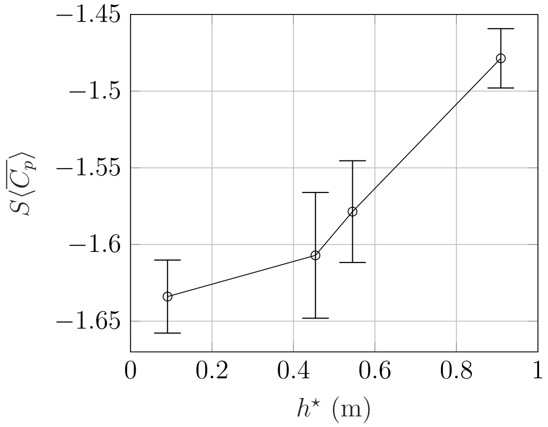

Fig. 23. Evolution of $S\langle\overline{C_p}\rangle$ with $h^\star$ for two slats free space configurations.

6. Conclusion

A measurement chain was developed to measure the pressure coefficient $\langle\overline{C_p}\rangle$ on the rear back of a full tractor–trailer vehicle on a test track. A device allowing to obtain a stable and known reference pressure for the differential sensor was designed. The reference pressure was measured in a sealed tank connected to the roof of the trailer, which also enabled the detection of wind gusts during the tests. This allowed an efficient discrimination of measurements where atmospheric conditions were not stable, and therefore with a non-stabilized reference pressure. Extensive measurements on a baseline case were carried out to determine the accuracy and repeatability of the measurements. The dispersion of $\langle\overline{C_p}\rangle$ was found to remain within 1.1% of the mean value of the pressure coefficient. Different underbody configurations were investigated by adding slats in the vertical plane of the rear back, allowing configurable opening ratio. It was found that the completely closed case presents a pressure distribution imputable to a class I flow, whereas configurations with large free space at the trailer rear correspond to class II flows. These results are consistent with small scale experiments, where the transition between class I and II flows occurs with increasing mass flow rate in the underbody. Regarding the drag force, the coefficient $S\langle\overline{C_p}\rangle$ is more likely driven by a change in the rear surface S than the pressure applying on it, for a progressive opening of the underbody. Configurations with constant open sections of 200 mm and 300 mm whose position is varied in the trailer rear plane were also considered. In both cases, $S\langle\overline{C_p}\rangle$ depends on $h^\star$, the vertical position of the openings, and relative variations up to 18% were found between a low and high opening. This finding aims at contributing to the proper placement of operative elements on the rear back of a trailer. They are a first step in the full-scale exploration of these effects and should be supplemented by unsteady pressure measurements and aerodynamic drag measurements on the complete truck.

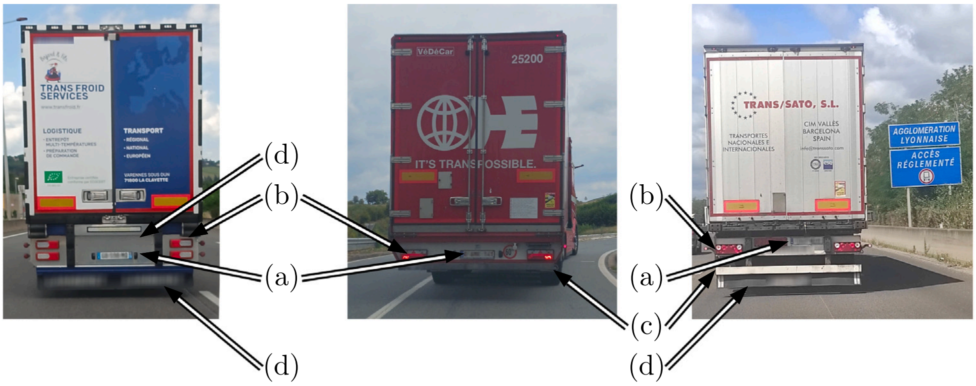

Fig. 24. Illustration of the variability of trailer rear underbody obstruction, showing the number plate location (a), rear lights (b), underrun protection device (c when visible) and additional devices (d).

CRediT authorship contribution statement

I. Kurek: Writing – review & editing, Writing – original draft, Methodology, Investigation, Formal analysis, Data curation, Conceptualization. **T. Castelain:** Writing – review & editing, Writing – original draft, Validation, Supervision, Resources, Project administration, Methodology, Investigation, Funding acquisition, Formal analysis, Data curation, Conceptualization. **M. Michard:** Writing – review & editing, Supervision, Methodology, Investigation, Funding acquisition, Data curation, Conceptualization. **D. Chacaton:** Writing – review & editing, Software, Project administration, Methodology, Formal analysis, Data curation, Conceptualization. **S. Bholah:** Resources, Project administration, Conceptualization. **B. Pellarin:** Resources, Conceptualization.

Declaration of competing interest

The authors declare that they have no known competing financial interests or personal relationships that could have appeared to influence the work reported in this paper.

Acknowledgments

This project was financed by the French government as part of France 2030. It is also supported by the Labex CeLyA of the Université de Lyon, operated by the ANR (ANR-10-LABX-0060/ANR-16-IDEX-0005).

Data availability

The authors do not have permission to share data.

References

Ahmed, D., Morgans, A.S., 2023. Wake bi-modality: The effect of upstream boundary layer dynamics. J. Fluid Mech. 975, A7.

Bonnavion, G., Cadot, O., 2018. Unstable wake dynamics of rectangular flat-backed bluff bodies with inclination and ground proximity. J. Fluid Mech. 854, 196–232.

Bonnavion, G., Cadot, O., Herbert, V., Parpais, S., Vigneron, R., Délery, J., 2019. Asymmetry and global instability of real minivans' wake. J. Wind Eng. Ind. Aerodyn. 184, 77–89.

Cadot, O., Evrard, A., Pastur, L., 2015. Imperfect supercritical bifurcation in a three-dimensional turbulent wake. Phys. Rev. E 91 (6), 063005.

Castelain, T., Michard, M., Szmigiel, M., Chacaton, D., Juvé, D., 2018. Identification of flow classes in the wake of a simplified truck model depending on the underbody velocity. J. Wind Eng. Ind. Aerodyn. 175, 352–363.

Cembalo, A., Borée, J., Coirault, P., Dumand, C., 2024. Large scale response of a vehicle wake to on-road perturbations. J. Wind Eng. Ind. Aerodyn. 255, 105933.

Copernicus Climate Change Service, 2024. Era5-land post-processed daily statistics from 1950 to present.

El-Alti, M., Chernoray, V., Kjellgren, P., Hjelm, L., Davidson, L., 2016. Computations and full-scale tests of active flow control applied on a volvo truck-trailer. In: Dillmann, A., Orellano, A. (Eds.), In: The Aerodynamics of Heavy Vehicles III, vol. 79, Springer International Publishing, Cham, pp. 253–267.

Fan, Y., Parezanović, V., Cadot, O., 2022. Wake transitions and steady z-instability of an ahmed body in varying flow conditions. J. Fluid Mech. 942, A22.

Gallagher, M., Morden, J., Baker, C., Soper, D., Quinn, A., Hemida, H., Sterling, M., 2018. Trains in crosswinds – comparison of full-scale on-train measurements, physical model tests and CFD calculations. J. Wind Eng. Ind. Aerodyn. 175, 428–444.

Grandemange, M., Gohlke, M., Cadot, O., 2013a. Bi-stability in the turbulent wake past parallelepiped bodies with various aspect ratios and wall effects. Phys. Fluids 25 (9), 095103.

Grandemange, M., Gohlke, M., Cadot, O., 2013b. Bi-stability in the turbulent wake past parallelepiped bodies with various aspect ratios and wall effects. Phys. Fluids 25 (9), 095103.

Grandemange, M., Ricot, D., Vartanian, C., Ruiz, T., Cadot, O., 2014. Characterisation of the flow past real road vehicles with blunt afterbodies. Int. J. Aerodyn. 4 (1/2), 24.

Haffner, Y., Borée, J., Spohn, A., Castelain, T., 2020. Mechanics of bluff body drag reduction during transient near-wake reversals. J. Fluid Mech. 894, A14.

Lahaye, A., Leroy, A., Kourta, A., 2014. Aerodynamic characterisation of a square back bluff body flow. Int. J. Aerodyn. 4 (1/2), 43.

Martini, H., Bergqvist, B., Hjelm, L., Löfdahl, L., 2011. Aerodynamic effects of roof deflector and cab side extenders for truck-trailer combinations. In: Commercial Vehicle Engineering Congress. Chicago, Illinois, United States, pages 2011–01–2284.

Plumejeau, B., Keirsbulck, L., Delprat, S., Lippert, M., Abassi, W., 2020. Behavior of the square-back ahmed body global modes at low ground clearance. Phys. Rev. Fluids 5 (8), 084701.

Rao, A.N., Minelli, G., Zhang, J., Basara, B., Krajnović, S., 2018. Investigation of the near-wake flow topology of a simplified heavy vehicle using PANS simulations. J. Wind Eng. Ind. Aerodyn. 183, 243–272.

Szmigiel, M., 2017. Effet du flux de soubassement sur la dynamique du sillage d'un corps non profilé à culot droit. Application du contrôle actif pour la réduction de traînée de véhicule industriel. (Ph.D. thesis). Université de Lyon.

Wojciak, J.D., 2012. Quantitative Analysis of Vehicle Aerodynamics during Crosswind Gusts. (Ph.D. thesis).

Wordley, S., Saunders, J.W., 2008. On-road turbulence. SAE Int. J. Passeng. Cars - Mech. Syst. 1 (1), 341–360.